Towards superconducting spintronics with RuO2 and CrO2 nanowires

Prateek, K.

2

Long Range Proximity Effects & Domain Wall Physics

This is Chapter 2, which gives an overview over some of the fundamental concepts to be appreciated in the context of this Thesis.

2.1. Introduction

As was already mentioned in Chapter 1, the major motivation to work on CrO_2 and RuO_2 nanowires lies in the fact that CrO_2 is a half-metallic ferromagnet, a class of materials that is uniquely suited to studying superconducting long range proximity effects and spin-polarized supercurrents. Even though this research was not successful, it is fitting to briefly reiterate the framework of the research question on the superconducting side, discuss some basic aspects of superconducting Josephson junctions, and mention what appeared to be the state of the art when the research started. This will be the first part of this Chapter. Then, for the final goal of having supercurrents interact with magnetic structures such as nanomagnets or domain walls (DWs), this Thesis presents results on the magnetic behavior of CrO_2 nanowires, and on pinning and depinning of DWs from constrictions in such nanowires. Some basic notions of magnetism and DW formation are therefore presented in the second part of this Chapter.

2.2. Superconductivity

2.2.1. General concepts

Superconductors are materials that transport electric charge without resistance. It is a so-called macroscopic quantum phenomenon, displaying, for instance, spontaneous flux expulsion and magnetic flux quantization. These quantum phenomena are associated with macroscopic wave functions characteristic of off-diagonal long-range order (ODLRO), a concept first introduced by Yang [1]. This order is characterized by a long-range coherence of the quantum mechanical phase which demonstrates itself in the form of macroscopic quantum phenomena. As a consequence of macroscopic occupation, a simple wave function Ψ can describe the whole superconducting state :

$$\Psi(r,t) = \sqrt{n_s(r,t)}e^{i\theta(r,t)} \tag{2.1}$$

where, n_s is the density of Cooper pairs and θ is the gauge covariant phase. $n_s = n_e/2$, where n_e is the normal electron density. A basic parameter characterizing a superconductor is the Ginzburg-Landau coherence length ξ_{GL}, which determines the distance over which the density of superconducting carriers can meaningfully change. The size of ξ_{GL} can vary from several tens of nm in metallic superconductors down to about 1 nm in the 'high critical temperature (T_c)' copper-oxide superconductors (HTS). The other important length scale is the London penetration depth λ_L which describes the decay of an external magnetic field from the edge of a superconductor toward its interior, from which it is ultimately

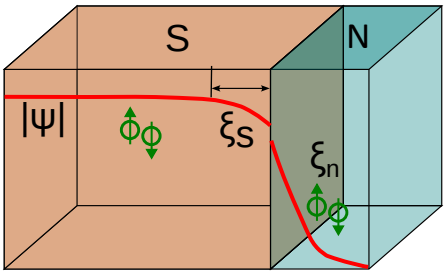

Figure 2.1: Schematic representation of the proximity effect between a superconductor (S) and a normal metal (N). The superconducting order parameter decays over the length scales ξ_S and ξ_N as it extends across the interface. The discontinuity of the order parameter at the interface signifies a non-perfect interface transparency.

expelled. The ratio ($\kappa = \lambda_L/\xi_{GL}$) between these two lengths bifurcates between two types of superconductors, type I, where flux expulsion below T_c is complete, and type II, where flux quanta (vortices) can remain present in the bulk of the material. Both ξ_{GL} and λ_L are temperature dependent. According to Ginzburg-Landau theory, $\xi_{GL}(T) = \xi_{GL}(0)(1 - T/T_c)^{-1/2}$, which implies a diverging enhancement of $\xi_{GL}(T)$ from its minimal value $\xi_{GL}(0)$ at T = 0 when T_c is approached. Similarly, $\lambda_L(T) = \lambda_L(0)(1 - (T/T_c)^4)^{-1/2}$. For λ_L, it is important to know that for film thicknesses $t \leq \lambda_L(T)$, $\lambda_L(T)$ has to be replaced by an effective penetration depth (also called Pearl length) $\Lambda(T) = 2\lambda_L(T)^2/t$.

2.2.2. Proximity effect with normal metals

In a superconductor (S) the electrons are ordered as Cooper pairs whereas in a normal metal (N), the electron arrangement lacks such pairing and is instead characterized by a continuous distribution of single-electron states that are filled up to the Fermi surface. When S is placed next to N, the electron ordering in the two systems does not undergo an instantaneous change at the interface, rather it happens over a finite distance. The characteristic length scale ξ over which the order parameter can change its magnitude is called the coherence length, which is a material property. At the side of N, an often-used picture is that Cooper pairs are carried over ('leak') into the metal and that their density decays over a length ξ_n (see Fig. 2.1). In a diffusive system, defined by $\xi_N < l_e$, where l_e is the electronic mean free path, ξ_N is given by

$$\xi_N = \sqrt{\frac{\hbar D_n}{k_B T}} \tag{2.2}$$

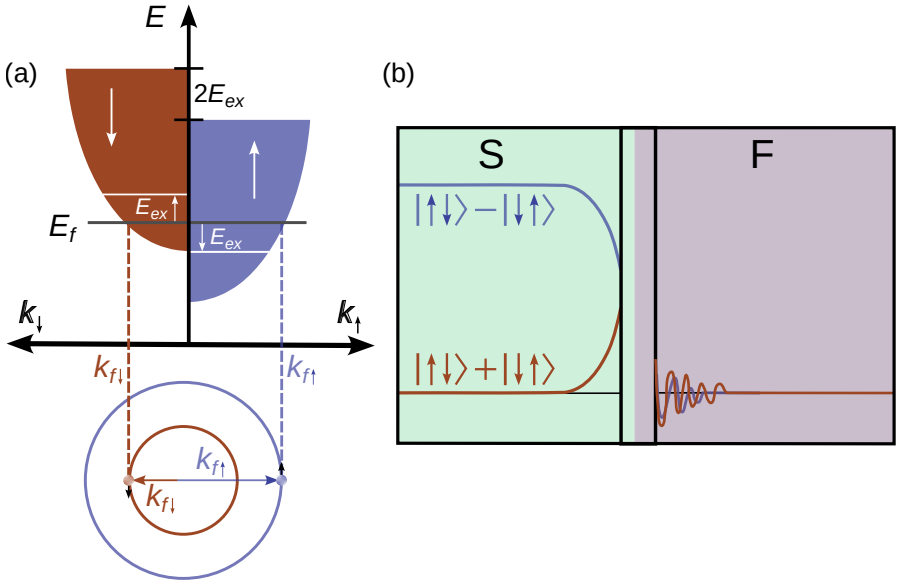

Figure 2.2: (a) Schematic representation of the electronic band structure for a ferromagnet. At S/F interface singlets have to adjust to Fermi energy E_F resulting in finite momentum. (b) Singlet (blue)-triplet (brown) mixing at S/F interface. Due to E_{ex} the correlations decay over very short distances resulting in short range proximity effect. The reflections from F layer cause spin-dependent phase shifts at S-side. Adapted from [2].

where $\hbar$ is reduced Planck constant, D_n is the diffusion coefficient of the metal, and k_B is the Boltzmann constant. ξ_N can be of the order of hundreds of nm. At the S side : As shown in Fig. 2.1 near the interface, the order parameter is depleted over a distance defined by $\xi_S(T)$, where $\xi(0)$ is the coherence length of S at T = 0 K. Therefore, the proximity effect is used to describe the induced superconductivity in a normal metal. Since the total condensate remains conserved, the Cooper pairs are "drained" from S which results in a suppression of T_c of the superconductor. We note in passing that there is another way to look at the superconducting correlations on the N-side of the interface, using the concept of Andreev reflections. In that language, the coherence on the N-side is rather furnished by an electron with a certain spin, coupled to a 'retroreflected hole' of opposite spin. Both pictures allow to discuss the coupling of two superconductors in an S/N/S geometry.

2.2.3. Proximity effect with ferromagnets

If the non-S metal is a ferromagnet (F) instead of a normal metal, several details change in the picture of the proximity effect. As previously mentioned in Ch. 1, the

exchange field E_{ex} of F splits the band structure for up and down spins, resulting in an energy shift of $2E_{ex}$. The singlet Cooper pairs consist of two electrons with equal and opposing momentum (k_F, -k_F) and spin ($\uparrow,\downarrow$). E_{ex} induces a momentum shift of $\pm\mathbf{Q}/2$ for electrons located at the Fermi level. In the diffusive limit Q = $2E_{ex}/\hbar v_F$, where v_F is the Fermi velocity. As a result, a finite momentum for $|\uparrow\downarrow\rangle$ may be expressed as $\mathbf{k}_{F\uparrow}$ - $\mathbf{k}_{F\downarrow} = \mathbf{Q}$, and for $|\downarrow\uparrow\rangle$ is $\mathbf{k}_{F\downarrow}$ - $\mathbf{k}_{F\uparrow} = -\mathbf{Q}$. This results in singlet Cooper pairs at the Fermi energy E_F acquiring a non-zero center-of-mass momentum. Consequently, a spin-mixed state emerges:

$$|\uparrow\downarrow - \uparrow\downarrow\rangle \implies |\uparrow\downarrow\rangle e^{i\mathbf{Q}\cdot\mathbf{R}} - |\downarrow\uparrow\rangle e^{i\mathbf{Q}\cdot\mathbf{R}} = |\uparrow\downarrow - \uparrow\downarrow\rangle\cos(\mathbf{Q}\cdot\mathbf{R}) + i|\uparrow\downarrow + \uparrow\downarrow\rangle\sin(\mathbf{Q}\cdot\mathbf{R}) \quad (2.3)$$

The first component represents a zero-spin oscillating singlet state ($S = 0$ while the second term defines a triplet state ($S = 1$) with a spin projection ($m_s = 0$) relative to the spin quantization axis, determined by the E_{ex}. These correlations can only persist in the F layer within a certain length scale from the interface. The decoherence length ξ_F over which all pair amplitudes decay exponentially is expressed as

$$\xi_F = \sqrt{\frac{\hbar D_F}{E_{ex}}} \quad (2.4)$$

in a diffusive limit. For a conventional F like Co, Ni ξ_F is only a few nm. For a 100% spin polarized material such as CrO_2, only one spin band is occupied at E_F in which case the singlets cannot be injected at all. In terms of Andreev reflections, there is no retroreflected hole with opposite spin available. As a consequence, the S/F interface is fully reflective and ξ_F is of the order of atomic distances. At the S side of the interface, stronger spin polarization of F causes a spin-dependent phase shifts ($\pm\theta$), forming a spin triplet mixture ($m_s = 0$) in S which increases with the spin polarization. E_{ex} results in different scattering phase delay which can be expressed as

$$|\uparrow\downarrow\rangle e^{i\theta} - |\downarrow\uparrow\rangle e^{i\theta} = |\uparrow\downarrow - \uparrow\downarrow\rangle\cos(\theta) + i|\uparrow\downarrow + \uparrow\downarrow\rangle\sin(\theta) \quad (2.5)$$

The oscillating dependence of the order parameter on the distance from S/F interface has an interesting implication: there is the possibility of a 0-π transition by varying the thickness of F layer [3, 4] or changing the temperature [5]. However, the short range of a few nm of the spin mixed state in F limits the development of applications.

2.2.4. Equal spin triplets and the Long-range proximity effect

The proximity effect in S/F hybrids is not restricted to short ranges. The quantization axis of correlations with zero spin projection can be rotated to produce alternative (equal spin) triplet correlations with $m_s = 1$(or -1). A ferromagnet does not break

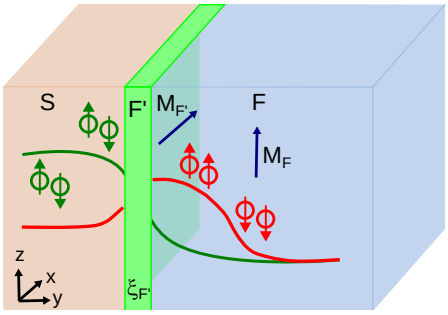

Figure 2.3: (a) Schematic representation of long range proximity effect in a S/F'/F hybrid. When magnetization of F' is non-collinear with F, the $m_s = 0$ triplet is rotated in the spin space and converted into equal spin triplet ($m_s = 1$). when $M_{F'}$ is $\perp$ to M_F singlet to triplet conversion is optimized. Equal spin pairs are not broken by E_{ex} and can exist up to hundreds of nm in F layer.

up equal spin triplets, denoted as $|\uparrow\uparrow\rangle$ and $|\downarrow\downarrow\rangle$ in Dirac notation. The rotation can come about by introducing magnetic non-collinearity or inhomogeneity at the S/F interface. One way to do that is by stacking a thin layer (within length ξ_F) of a magnetic material F' with a different magnetization direction than F (see Fig. 2.3) [6, 7]. For instance, we assume $M_{F'}$ to align with the x-axis while M_F is along z. The spin mixing in S due to F' is then a consequence of E_{ex} along x. The magnetization of spin mixing correlations gets rotated to z. The triplet state ($m_s = 0$) has zero-spin projection along x but it can have non-zero component $|\uparrow\uparrow\rangle_z$ and $|\downarrow\downarrow\rangle_z$ along z. The amount of spin polarization of F and the degree of magnetic inhomogeneity defines the relative amplitude of the two components. In case of half-metals, one of the two is completely suppressed. Due to their equal spins, the triplets are not affected by E_{ex} and therefore can stay coherent over large distance, similar to singlets in a normal metal, resulting in a Long Range Proximity effect. The main limiting factor here is the spin diffusion length, while the characteristic decay length is given by

$$\xi_F^T = \sqrt{\frac{\hbar D_F}{k_B T}} \tag{2.6}$$

In conventional F metals, ξ_F^T can be tens of nanometers. However for 100% spin polarized F like CrO_2 spin flipping is not an issue and ξ_F^T can be several hundreds nanometers. The equal spin triplet supercurrents are by definition spin-polarized. They offer great potential for the development of superconducting electronics wherein not only the charge and the superconducting phase, but also the spin is utilised. The primary focus of our study revolves around two systems, namely Josephson junctions and triplet spin valves. In the following sections an overview of the general Josephson effect is given prior to the examination of earlier studies on proximity effects.

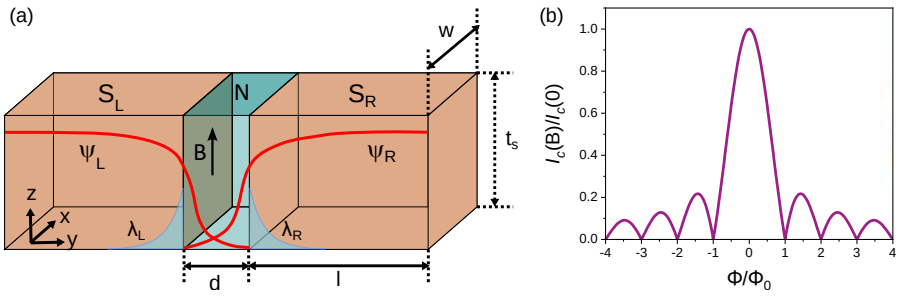

Figure 2.4: (a) Schematic representation of a Josephson junction : Two superconducting (S) electrodes (orange) separated by a thin weak link (blue) of length d. The amplitude of two superconducting wave functions (red) is shown to be overlapping, resulting in a supercurrent through the junction. The dimensions of the superconductors are : width (w), thickness (t_s), length (l). The magnetic field is applied along the z-axis and the current flow is along the y-axis. The magnetic field penetrates into S and decays exponentially over the London penetration depth (λ_L, λ_R).(b) The Fraunhofer-like interference pattern of the critical current I_c in a JJ due to the applied field, in units of flux normalized by the flux quantum. The central peak is two times wider than the side lobes, and the side lobe maxima decay as 1/B.

2.2.5. Josephson junctions

The Josephson effect in general describes the transfer of Cooper pairs and the coupling of the macroscopic wave functions between two superconductors via a weak link. The nature of the weak link determines the transport through the junction and can be insulating (I), a normal metal (N) or a ferromagnet (F). A schematic of such a geometry is given in Fig. 2.4(a) which shows two superconducting electrodes, each corresponding to a distinct wave function described by $\Psi_{L,R} = \sqrt{n_{s_{L,R}}} e^{i\theta_{L,R}}$ separated by a thin N layer such that the two wave functions overlap and maintain coherence. We assume that the density of Cooper pairs (n_s) stays the same in both the electrodes. The phase difference φ between the two condensates is given by $\theta(L) - \theta(R)$, where $\theta(L,R)$ corresponds to the phase of the individual condensates. Supercurrents in the weak link are driven by the phase difference and can be expressed as

$$J = J_c \sin(\varphi) \tag{2.7}$$

J_c is the maximum current density the junction can sustain. Above this current, the junction returns to the normal resistive state and a finite voltage is measured. The sinusoidal current-phase relation reveals the wave-like nature of the charge transport in a superconductor. The manifestation of quantum behavior becomes more apparent when a magnetic field is applied in a direction perpendicular to the current. Experimentally, it results in a "Fraunhofer"-like diffraction pattern (see Fig. 2.4(b)) similar to the diffraction pattern observed when a wave passes through a single slit. It is also called as superconducting quantum interference (SQI) pattern. When an external field is applied, the vector potential interacts with the

supercurrent, resulting in the introduction of an additional phase difference that is proportional to the strength of the field. The critical current exhibits oscillatory behavior when the field is increased due to the periodicity of the phase, superimposed on the decay due to orbital breaking effect. The periodicity of the oscillation is equal to $\Delta B = \Phi_0 / A$, where Φ_0 is the magnetic flux quantum and A is the effective junction area, given by $(\lambda_L + \lambda_R + d)\, w$ (see Fig. 2.4(a)), penetrated by the flux (Φ). The SQI is described by

$$\frac{I_c(B)}{I_c(0)} = \left| \frac{\sin(\frac{\pi\Phi}{\Phi_0})}{\frac{\pi\Phi}{\Phi_0}} \right| \tag{2.8}$$

It should be noted that the periodicity of SQI is dependent on the size of the superconductor. The above discussion holds true under the condition that the thickness t of S is larger than the London penetration depth λ. As discussed in the previous sec. 2.2 (and shown in Fig. 2.4(a)) the magnetic field applied along the z axis decays in both right and left superconducting electrodes over λ. In particular, junction physics becomes different when the thickness of the superconducting electrodes is less than λ. Additionally, when the junction width w becomes smaller than the Josephson penetration length ℓ_J given by

$$\ell_J = \frac{\Phi_0}{4\pi\mu_0\lambda^2 J_c(0)} \tag{2.9}$$

with J_c being the (presumed homogeneous) critical current density of the junction. The shielding current running along the junction, responsible for the shape and periodicity of SQI is no longer determined by Meissner effect. In this scenario, as has been discussed in numerous studies, the electrodynamics becomes non-local, and $I_c(B)$ becomes independent of λ and is solely determined by the geometry of the device [8–12]. In particular, when $l >> w$ then $\Delta B = 1.84\Phi_0 / w^2$ and when $l << w$ then $\Delta B = 2\Phi_0 / (l \cdot w)$.

2.2.6. Earlier work on proximity effect in CrO_2

A first experimental breakthrough in long-range effects came in 2006, when Keizer et al. reported a Josephson supercurrent between two singlet superconducting electrodes (NbTiN) separated by (0.3- 1) μm of CrO_2 film[13]. The half-metallic nature of CrO_2 completely suppresses the Andreev reflections, hence preventing the penetration of singlet Cooper pairs, and the supercurrent was strong evidence for the LRP effect. They found a critical current density of the order of 5×10^9 A/m^2 and also observed SQI when an in-plane transverse field to the current was applied. Their experiments however, did not provide information about the pairing symmetry of the correlations. Furthermore, they reported large spread in their critical currents which suggests that the triplet generator was poorly defined and controlled.

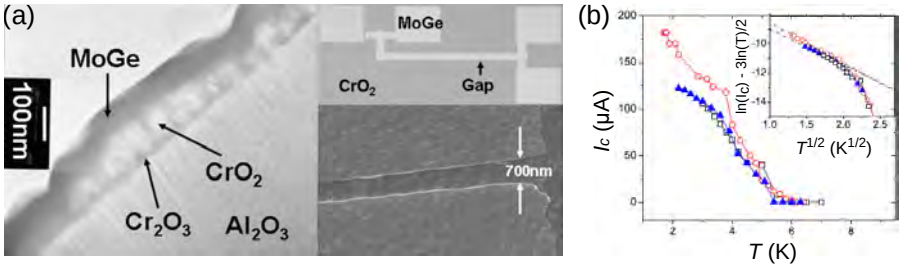

Figure 2.5: (a) (left) Transmission electron microscopy image of a CrO_2 film grown on Al_2O_3. Visible are the Cr_2O_3 seed layer, the CrO_2 layer, and the MoGe layer. (right) Layout of the device structure with four current/voltage contacts. The width of the electrodes is 30 μ m. SEM image of the gap between the two electrodes of 700 nm, made by liftoff. (b) Critical current I_c versus temperature T for three different junctions. The inset shows a linear fit to a plot of $\ln I_c - 3/2 \ln T$ vs $\sqrt{T}$. Taken from Ref. [14].

In 2010, Anwar et al. were able to successfully replicate the effect using MoGe electrodes separated by 700 nm on CrO_2 film grown on a Al_2O_3 substrate [14]. They observed supercurrents of the order of 10^7 A/m^2, lower by two order of magnitude compared to the previous study. Furthermore, it was estimated that the supercurrents were limited to a thickness of around 30 nm out of 100 nm of CrO_2 film resulting in a weaker junction. It was argued, supported by TEM images (see Fig. 2.5(a)), that the growth of CrO_2 films on Al_2O_3 leads to significant differences in film morphology: growth on Al_2O_3 does not start as CrO_2, but rather as Cr_2O_3 and only after a few tens of nanometers, the growing film becomes CrO_2.

One way to estimate the strength of a junction is by measuring the critical current I_c as a function of temperature. In a diffusive limit, for a long junction $I_c \propto T^{3/2} e^{\sqrt{(2\pi K_B T)/E_{Th}}}$, with E_{Th} the Thouless energy. Their junction showed good compliance at low temperatures up to 2 K (see Fig. 2.5(b)) with values of E_{Th} around 72 μV. However, no clear Fraunhofer pattern was observed when an in-plane magnetic field is applied parallel to the I_c. Furthermore, I_c showed little sensitivity to applied fields up to 500 mT which suggested that the non-collinear magnetic moments responsible for triplet generation are pinned at the CrO_2 interface. The authors also found a high normal state resistance R_N of 11 Ω instead of expected value of 4 mΩ which pointed to a low transparency of the S/F interface. This was due to the fact that CrO_2 is metastable and reduces to Cr_2O_3 at room temperature. This forms an insulating layer and has to be Ar-etched away before the superconducting electrodes are deposited. The Ar etching will not only remove unwanted oxides but may also damage the surface.

Overall, the complicated fabrication process to get the desired interface transparency and the lack of control over magnetization at the interface with CrO_2 films

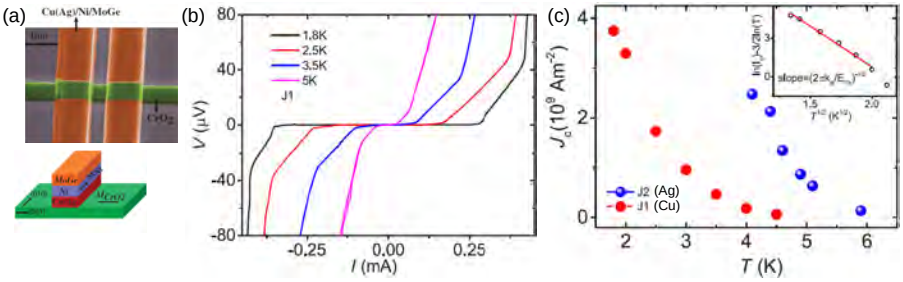

Figure 2.6: (a) Scanning electron micrograph (false color) of a Josephson junction on a CrO2 nanowire (green), Orange contact pads consist of trilayer (Cu or Ag)/Ni/MoGe. (top). Schematic of the device with CrO_2 wire as a weak link. (b) Current I versus voltage V characteristics of J1 at different temperatures. (c) Critical current density Jc vs T. The inset shows a linear fit to a plot of $\ln I_c - 3/2 \ln T$ vs $\sqrt{T}$. Taken from Ref. [16].

revealed the some of the limitations of these junctions. Consequently, the proportion of fabricated junctions exhibiting supercurrents falls below 30%.

In 2012 Anwar et al. improved on their previous work and reported supercurrents on CrO_2 films grown on TiO_2 substrates by employing a sandwich layer of Ni/Cu between the CrO_2 film and superconducting MoGe [15]. Adding a thin ferromagnetic layer of Ni layer provided the necessary magnetic inhomogeneity for triplet generation similar to the model proposed by Houzet and Budzin[6]. They observed an I_c of the order of 10^9 A/m^2, comparable to ref. [13] and two order of magnitude more than junctions on Al_2O_3 substrates. However, other issues like no clear Fraunhofer pattern in the presence of an external field, non-zero I_c at fields of 500 mT suggesting that the lack of control of magnetization at the interface and low interface transparency still remained.

So far, the studies were conducted on 'full-film' devices which, as we discussed, suffer from limitations due to presence of grain boundaries, ill-defined current paths and an lack of control of the magnetization state at the local level. In 2016, Singh et. al. reported selective area grown CrO_2 nanowires based lateral JJs[16]. Similar to the above studies, artificial magnetic homogeneity was provided by a sandwich layer of Cu (or Ag)/Ni at the interface of CrO_2 and MoGe (see Fig. 2.6(a)). It was observed that these junctions could also sustain supercurrents of the order of 10^9 A/m^2 below 5 K for a junction length of 500 nm. Furthermore, the junctions which used Ag (J2) instead of Cu (J1) had a larger critical current density (see Fig. 2.6(c)). It was postulated that the observed improvement in performance can be attributed to the increased interface transparency resulting from the use of Ag which, unlike Cu, does not undergo oxidation at the contact with CrO_2. The Thouless energy was estimated to be around 11 μV from the slope of plot (inset Fig. 2.6(c)), which was in good agreement with the calculated value of 15 μV using the relationship $E_{Th} = \hbar D/L^2$

where, diffusion constant D = 3.7×10^{-3} m^2/s and junction length L = 400 nm.

It can be concluded from these studies that selective area growth of CrO_2 nanowires with a well defined geometry and magnetization allows to overcome some of the issues of earlier studies on films. The estimated current densities are large enough to envision devices where such spin-polarized supercurrents could be used to manipulate the magnetization of a nanomagnet [17]. This forms the motivation behind the current work.

2.3. Magnets and magnetic domains

2.3.1. A magnetized object: The Landau free energy

Magnetic materials, such as ferromagnets, ferrimagnets, etc., contain regions where spins cluster to create uniform magnetization. These regions, known as magnetic domains, were first postulated by Weiss to explain extremely high permeability in the ferromagnets [18]. The development of the Weiss molecular field, which is actually a manifestation of the exchange interaction, was part of the solution, while the other part was the assumption that the sample was divided into multiple fully magnetized regions, called magnetic domains. The presence of magnetic domains was first suggested by the experimental work of Barkhausen [19] but it was confirmed later by Sixtus and Tonks [20] and Bitter [21]. Later, in 1935, Landau and Lifschitz proposed that the formation of magnetic domains in ferromagnetic materials helps to minimize the magnetostatic energy [22], along with the domain wall profile which was an improvement on Bloch [23] and Heisenberg work [24]. The fundamental concepts of magnetic domains were reviewed by Kittel [25], and later Hubert and Schäfer [26] extended the theory beyond the magnetostatic energy to include additional energy components.

The competition between the different energy terms that describe a magnetic object provides the physical foundation for domain formation. The sum of the individual energy contributions is the Landau free energy (G_L), given by the sum of the exchange energy E_{ex}, the Zeeman energy E_Z, the anisotropy energy E_{aniso} and the magnetostatic energy (also called the magnetostatic self-energy) E_{ms} [27]

$$G_L = E_{ex} + E_Z + E_{aniso} + E_{ms} \tag{2.10}$$

As with all physical systems, the magnetic system seeks to minimize this Landau free energy. Since the magnitude of the magnetization vector is fixed, its direction must be changed. To determine the magnetization direction with the lowest total energy, a compromise must be reached between these energy terms. Consequently, some spins will no longer be pointing along this optimal direction. Typically, a uniformly

magnetized state has a high magnetostatic energy (Fig. 2.7(a)) (Fig. 2.7(a)), which can be reduced by forming a non-uniform or even flux-closed magnetic state (Fig. 2.7(b-d)). The formation of domains continues until the decrease in magnetostatic energy is balanced by the exchange and anisotropy energy costs, accompanied by magnetic structure twists and deviations. If an external magnetic field is applied, the Zeeman energy also plays a role which may be sufficient to eliminate the domain state and generate a uniform saturated state. [28, 29]. Detailed expressions for these energy contributions can be written down in terms of volume integrals over local energies that in turn involve local fields, local magnetic moments $\vec{m}(\vec{r})$ and spatial gradients of $\vec{m}$. Parameters involved in determining the size of each contribution are as follows :

(i) for E_{ex} it is the exchange stiffness which tries to align neighboring spins and is related to J: $A \propto kJS^2/a_0$, where J is the nearest neighbor exchange constant, S is the spin magnitude, a_0 is the lattice constant, and k is a numerical factor depending on the lattice symmetry [30];

(ii) for E_Z it is the saturation magnetization M_s of the object;

(iii) for E_{ani} it is a general parameter $\varepsilon_{ani}(\vec{m}(\vec{r}))$. Magnetocrystalline anisotropy results from the orbital coupling of the crystal structure and the spin moments via spin-orbit coupling. It depends on the crystal symmetry and any defects in the crystal lattice would cause a change in anisotropy. A way to handle this is to express ε_{ani} in terms of the angles α_i between the magnetization and the crystal axes. For uniaxial anisotropy, that leads to an expression of the form $\varepsilon_{ani}(\vec{m}(\vec{r})) = K_0 + K_1 \cos^2(2\alpha) + \ldots$;

(iv) for E_{ms} there is no parameter that sets the scale. It represents the energy cost of magnetic poles on the surface due to stray magnetic fields leaving the material and therefore depends on the shape of the sample (shape anisotropy). The fields created by the sample also lead to an internal field H_i that is different from the applied field, but also not simply given by the magnetization. It can be written as $\vec{H}_i = \vec{H}_a + \vec{H}_d$, where $\vec{H}_d$ is the so-called demagnetization field, that will depend on the sample shape. This shape dependence is the reason that the magnetization becomes non-uniform, meaning that magnetic domains form, for non-ellipsoidal objects.

This leads to an expression for the Landau free energy that reads:

$$G(\vec{M}) = \int_V \left(A(\nabla \vec{m})^2 - \mu_0 M_s(\vec{H}(\vec{r}) \cdot \vec{m}(\vec{r})) + \varepsilon_{ani}(\vec{m}(\vec{r})) - \frac{\mu_0}{2}(\vec{H}_d \cdot \vec{M}) \right) dV \quad (2.11)$$

The local minima of the G_L can be determined by varying the system's magnetization configuration and satisfying the necessary conditions for the existence of a

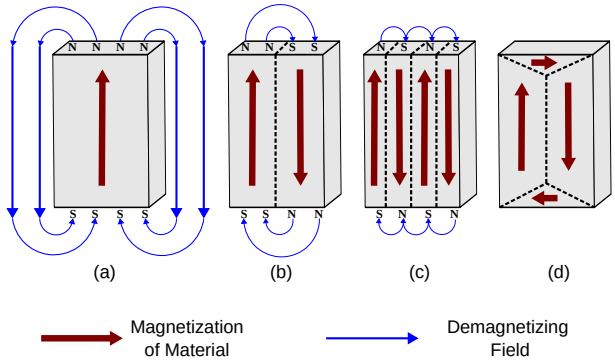

Figure 2.7: Schematic illustration of the breaking up and formation of magnetic domains (a) single domain state with uniform magnetization, (b) two-domain state with reduced magnetostatic energy, (c) four-domain state with even lower magnetostatic energy, and (d) a flux-closure domain state with zero magnetostatic energy (adapted from ref. [31]).

minimum. Stable magnetization configurations should then follow from finding free energy minima through solving the variational problem $\frac{\delta G}{\delta M} = 0$ with appropriate boundary conditions.

This works for a uniform magnetization, but does not simply allow to find configurations where different domains of the object have different directions of the magnetization. Domain theory tries to make this complexity easier to deal with. It proposes that in a macroscopic sample is subdivided in such domains that are separated by planar regions where the magnetization is changing its direction. These regions are called Domain Walls (DWs). Figure 2.7 illustrates the principle, showing how domain formation minimizes the stray fields and their energy. One point to keep in mind is that the gain is in the stray fields, but the loss is in exchange energy. If the separation between domains would be a single-atom-width plane, the exchange energy price is very high, because spins have to be fully flipped. In practice, the DW therefore will have a finite width. In the next section we look into DWs in more detail.

2.3.2. Domain Walls

Generally, there is a narrow transition region between magnetic domains where the direction of the magnetization vector varies continuously. As mentioned above, it is energetically (much) more favorable to rotate the magnetic moments gradually over the DW region. In this thesis, we will work with DWs in which the magnetization vector can rotate in one of the two ways – either in the plane of the wall, or out of that plane. These two possibilities are referred to as either a Bloch wall [23] or a

Néel wall [32], respectively. The former is more prevalent in bulk materials such as thick films, whose magnetization vector rotates parallel to the wall plane, whereas the latter is preferred for thin films, whose magnetization vector rotates in the wall plane. They will be discussed in details below.

Bloch Wall : Felix Bloch proposed the Bloch wall. Subsequently, Landau and Lifshitz analyzed its properties in greater detail. It is found in bulk materials since, despite the rotation of the magnetization vector, the condition $\nabla \cdot \vec{M} = 0$ is satisfied everywhere including the wall. This means that there is no charge associated with the wall, hence no stray field, and no magnetostatic energy cost associated with the creation of the wall. However, the exchange energy term incurs an additional cost since the neighboring magnetic moments are no longer parallel. To achieve a low magnetocrystalline energy, the magnetization within the domains prefers to align along the easy axis direction, so there will be some anisotropy cost to the wall as well as the magnetisation must rotate through a hard direction. The width of the DW δ_w is given by

$$\delta_w = \pi \sqrt{\frac{A}{K}} \tag{2.12}$$

where, A is the exchange stiffness constant and K is the anisotropy constant. The DW energy per unit area, which is the energy cost of creation of a DW per unit area in terms of the exchange and anisotropy contributions only is expressed as

$$\sigma_W = 2\pi\sqrt{AK} \tag{2.13}$$

Néel Wall : Louis Néel proposed that in thin film systems, the energy costs are different than in the bulk materials. Typically, the magnetization within the domains lies in the film plane; however, for a Bloch wall to form, the magnetization must rotate out of the film plane. This will result in surface charges or stray field and extra cost in magnetostatic energy which increases as the sample thickness decreases. Therefore, in order to reduce this energy in thin films, the magnetic moments inside the wall may rotate in the surface plane, as shown in Fig. 2.7. Such a DW is called Néel wall. Néel walls are only stable in films thinner than the wall width and it can be approximated by an elliptical cylinder of cross section $t \times \delta_w$ where t is the film thickness and δ_w is the width of the DW. The wall profile for the Néel wall is given by [33]

$$\theta(x) = 2\arctan\left(\exp\left(\frac{x - x_0}{\delta_w}\right)\right) \tag{2.14}$$

where, θ is the angle of the local magnetization in the wall, x the position along the nanowire and x_0 the central position of the DW. The DW energy is now given by

$$\sigma_w = 4\sqrt{AK} \tag{2.15}$$

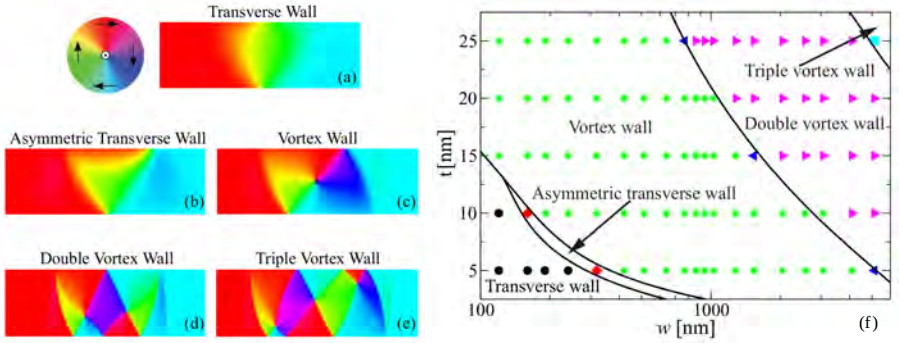

Figure 2.8: Equilibrium micromagnetic domain wall structures encountered in a Permalloy (Py) nanowire of a wide range of thicknesses and widths. TW for w = 120 nm and t = 5 nm, b) ATW for w = 160 nm and t = 10 nm, c) VW for w = 640 nm and t = 15 nm, d) DVW for w = 2560 nm and t = 20 nm, and e) TVW for w = 5120 nm and t = 25 nm. The color wheel (top left) shows the mapping between magnetization directions and colors. w,t correspond to the width and thickness of the wire respectively. Simulations were performed using Mumax3. (f) Phase diagram corresponding to the type of domain wall as a function of the width and thickness in a Py nanowire. (Image from Ref. [35]).

and the wall width by

$$\delta_w = \sqrt{\frac{A}{K}} \tag{2.16}$$

For a bulk sample the demagnetizing factor for the Bloch wall is zero, while that for the Néel wall is 1 [34].

Other types of walls which are some form of combination of Bloch and/or Néel also exist that could result in having lower energy than Bloch or Néel walls depending on thickness, external field value etc. Some of the more common examples, but not relevant to this thesis, are cross-tie walls, asymmetric walls etc.

2.4. Magnetization Dynamics

In the preceding sec.2.3 we discussed the energy contributions that influence the equilibrium state of the magnetic moments in a sample. However, it only provides a static solution for the magnetization distribution and the dynamical behavior of a system, such as its response to a change in the external field or the injection of a current, has not yet been included. Landau-Lifshitz-Gilbert equation which describes magnetization dynamics provides the solution to this problem. Additionally, some extensions are proposed to describe interactions with spin-polarized electric currents.

2.4.1. The Landau-Lifshitz-Gilbert Equation

The Landau-Lifshitz-Gilbert (LLG) equation initially proposed by Landau and Lifshitz [22] and later modified by Gilbert [36], mathematically describes the temporal and spatial evolution of the magnetization under the influence of an effective magnetic field. The same equation can be used to understand both the magnetization reversal of a uniform magnetic domain and the magnetization dynamics inside the DW.
When an external magnetic field is applied to a magnetic material, the magnetization $\vec{M}$ starts to precess in a circular orbit around the field axis. The torque that causes this precession can be written as

$$\frac{\partial \vec{M}}{\partial t} = -\gamma \vec{M} \times \vec{H_{eff}} \tag{2.17}$$

Here, γ is the gyromagnetic ratio and is expressed as $\gamma = \frac{ge\mu_0}{2m_e}$ where, g is the Landé factor (~ 2) and $\vec{H_{eff}}$ is the effective field that induces a torque due to which the magnetization will start precessing at Larmor frequency given by $\omega_L = \gamma \left|\vec{H}_{eff}\right|$.
Taking into account only this torque, the magnetization should perpetually precess around the external field. Experimentally, this is not observed: when an external field is applied, the magnetization relaxes into an equilibrium state aligned along $\vec{H}_{eff}$. Consequently, an additional damping torque $\vec{T}_d$ is required to explain the magnetization dynamics. In the LLG formalization, damping is expressed as

$$\vec{T}_d = \frac{\alpha}{M_s} \vec{M} \times \frac{\partial \vec{M}}{\partial t} \tag{2.18}$$

where, α is the damping constant, $\alpha > 0$. The damping mechanism is associated with a transfer of energy from the magnetic system to other degrees of freedom such as the lattice through the spin-orbit coupling. Therefore, the LLG equation for the net magnetization dynamics can be written as the sum of two terms: a precessional term and damping term.

$$\frac{\partial \vec{M}}{\partial t} = -\gamma \vec{M} \times \vec{H}_{eff} + \frac{\alpha}{M_s} \vec{M} \times \frac{\partial \vec{M}}{\partial t} \tag{2.19}$$

2.4.2. Spin-transfer torque

The Landau-Lifshitz-Gilbert equation presented in eq. 2.19 describes magnetization dynamics, but no interactions with spin-polarized currents or spin currents. The microscopic origins of spin transfer torque are still a matter of debate. Present consensus holds that at least two mechanisms can cause DW motion by current, to be discussed next:

Adiabatic spin-transfer Conservation of spin angular momentum provides an intuitive explanation for the effect of current on domain wall motion. When the conduction electrons flow through a spin-polarized material, their spin align with the local magnetization of their environment due to the intratomic (Hund) exchange field interaction [37]. When such an electron crosses a domain wall, it senses a change in magnetization and realigns with the local magnetization inside the domain wall. This means that the system's total angular momentum has changed from its initial value. To compensate for this change, the first domain must expand, which corresponds to a movement of the domain wall in the direction of the electron flow. The mechanism behind this type of transfer is the s–d exchange force between the localized 3d-electrons in the domain wall and the delocalized 4s-electrons carrying the current ($\vec{S} \propto \vec{M}$) [38, 39].

$$H_{ex} = -J_{ex}\vec{s}\cdot\vec{S} \tag{2.20}$$

where, J_{ex} is the exchange coupling strength. This interaction generates a torque $\vec{\tau}$ that is responsible for the movement of the domain wall along the electron flow direction.
Li and Zhang [40] and Thiaville and Miltat [41] independently proposed similar extensions to the Landau–Lifshitz–Gilbert equation to describe the interaction with an electrical current, the extension differ only in their coefficients. Both groups proposed a spin–transfer torque term as a function of the generalized velocity $\vec{u}$ which can be expressed in terms of the current density J:

$$\vec{u} = \frac{g\mu_B P}{2eM_s}\vec{J} \tag{2.21}$$

where g is the Landé factor, μ_B the Bohr magneton, P the spin polarization, e the electron charge and M_s the saturation magnetization. According to the Li-Zhang model, the spin-transfer torque $\vec{\tau}_{adiabatic}$ is expressed as[40]:

$$\vec{\tau}_{adiabatic} = -\frac{\vec{M}}{M_s^2} \times (\vec{M} \times (\vec{u}\cdot\vec{\nabla}))\vec{M}) \tag{2.22}$$

According to the Thiaville-Miltat model, the spin-transfer torque is expressed as[41]:

$$\vec{\tau}_{adiabatic} = -(\vec{u}\cdot\vec{\nabla})\vec{M} \tag{2.23}$$

At low temperatures the magnetization vector $\vec{M}$ has a constant length, so then Eq.2.22 proposed by Li and Zhang is equivalent to the formulation of Thiaville and Miltat in Eq.2.23. Both models work only above the Walker breakdown field (the maximum external field at which the DW attains a maximum velocity) and coul not explain the experimentally observed continuous domain wall propagation for relatively low currents densities.

Non-adiabatic spin-transfer Considering only the adiabatic contribution, the predicted critical current density for domain wall motion is much larger than the experimentally observed value [41, 42]. An additional torque mechanism is required to correctly describe the experiments which results from the spatial mistracking of the conduction electron spins and the local moments. When the spin orientation of the conduction electrons does not match the spin direction of the local moments, the electrons can be reflected from the local moments, thereby altering their direction of motion. In turn, this can transfer linear momentum from the conduction electrons to the local moments, leading to DW motion. This mechanism is commonly referred to as the non-adiabatic spin transfer process, where non-adiabaticity represents the misdirection of the conduction electron spins and local moments.

Thiaville and Miltat proposed the following addition to the Landau-Lifshitz-Gilbert equation to quantify the mistracking between conduction electron spin and local magnetization [43]:

$$\vec{\tau}_{non-adiabatic} = \frac{\beta}{M_s}\vec{M} \times \left[(\vec{u}\cdot\vec{\nabla})\vec{M}\right] \tag{2.24}$$

where, β is the non-adiabaticity parameter and is identified as the squared ratio of the exchange length and spin flip length, $\beta = (\lambda_{ex}/\lambda_{sf})^2$ where λ is the associated diffusion length.
Zhang and Li provide a similar equation, but a more rigorous derivation from the semiclassical Bloch equation[38]. Zhang's version uses a slightly reduced $\vec{u}$ and defines β equal to the ratio of the exchange time and spin flip relaxation time ($\beta = \tau_{ex}/\tau_{sf}$), but otherwise the proposed extensions are identical.
The complete LLG equation for the current induced domain wall motion including both the adiabatic and non-adiabatic torques can be written as

$$\frac{\partial\vec{M}}{\partial t} = -\gamma\vec{M}\times\vec{H}_{eff} + \alpha\frac{\vec{M}}{M_s}\times\frac{\partial\vec{M}}{\partial t} - (\vec{u}\cdot\vec{\nabla})\vec{M} + \frac{\beta}{M_s}\vec{M}\times\left[(\vec{u}\cdot\vec{\nabla})\vec{M}\right] \tag{2.25}$$

These equations provide experimentalists various quantities to verify the theoretical descriptions. From the application point of view, the usefulness of the current induced DW motion depends on two parameters: the current required for the depinning of the DW and the DW velocity. For applications such as the racetrack memory [44], one is obviously interested in low critical current densities and high and reproducible domain wall velocities. Typical measured current densities on Py based structures are relatively high and of the order of 10^{12} A/m^2 [45–47]. By improving the sample quality (increasing nonadiabaticity), the depinning critical current could be decreased [48]. Another way could be by increasing spin polarization. When there are no pinning sites, the critical current is proportional to the hard-axis magnetic anisotropy [49], and depends on the spin polarization of the

current:

$$I_c = \left(\frac{2e}{\hbar}\right)\left(\frac{\alpha}{P}\right) V M_s (H_K + 2\pi M_s) \tag{2.26}$$

where α is Gibert damping parameter, P is the spin polarization of the current, V is the volume of the domain, M_s is the saturation magnetization and H_K is the anisotropy field [29, 50, 51]. Regarding the DW velocity, initial studies reported velocities of the order of 1 m/s [45, 46], but in high quality samples of Py, with the maximum applicable current density, STT-driven DW velocities were observed up to 100 m/s [52]. However, experimentally increasing the current density may lead to Joule heating in the sample and cause damage. Half metals like CrO_2 with 100% spin polarization are a natural choice to consider in the development of reliable domain wall motion and pinning technology.

References

[1] Yang, C. N. Concept of Off-Diagonal Long-Range Order and the Quantum Phases of Liquid He and of Superconductors. Rev. Mod. Phys. **34**, 694–704 (1962). URL https://link.aps.org/doi/10.1103/RevModPhys.34.694.

[2] Lahabi, K. Spin-triplet supercurrents of odd and even parity in nanostructured devices. Ph.D. thesis, Leiden University (2018).

[3] Kontos, T. et al. Josephson junction through a thin ferromagnetic layer: Negative coupling. Phys. Rev. Lett. **89**, 137007 (2002). URL https://link.aps.org/doi/10.1103/PhysRevLett.89.137007.

[4] Blum, Y., Tsukernik, A., Karpovski, M. & Palevski, A. Oscillations of the Superconducting Critical Current in Nb-Cu-Ni-Cu-Nb Junctions. Phys. Rev. Lett. **89**, 187004 (2002). URL https://link.aps.org/doi/10.1103/PhysRevLett.89.187004.

[5] Ryazanov, V. V. et al. Coupling of two superconductors through a ferromagnet: Evidence for a π junction. Phys. Rev. Lett. **86**, 2427–2430 (2001). URL https://link.aps.org/doi/10.1103/PhysRevLett.86.2427.

[6] Houzet, M. & Buzdin, A. I. Long range triplet josephson effect through a ferromagnetic trilayer. Physical Review B **76**, 060504 (2007).

[7] Halterman, K., Valls, O. T. & Barsic, P. H. Induced triplet pairing in clean *s*-wave superconductor/ferromagnet layered structures. Phys. Rev. B **77**, 174511 (2008). URL https://link.aps.org/doi/10.1103/PhysRevB.77.174511.

[8] Kogan, V. G., Dobrovitski, V. V., Clem, J. R., Matawari, Y. & Mints, R. G. Josephson junction in a thin film. Phys. Rev. B **63**, 144501 (2001). URL https://link.aps.org/doi/10.1103/PhysRevB.63.144501.

[9] Moshe, M., Kogan, V. G. & Mints, R. G. Edge-type josephson junctions in narrow thin-film strips. Phys. Rev. B **78**, 020510R (2008). URL https://link.aps.org/doi/10.1103/PhysRevB.78.020510.

[10] Clem, J. R. Josephson junctions in thin and narrow rectangular superconducting strips. Phys. Rev. B **81**, 144515 (2010). URL https://link.aps.org/doi/10.1103/PhysRevB.81.144515.

[11] Boris, A. A. et al. Evidence for nonlocal electrodynamics in planar josephson junctions. Phys. Rev. Lett. **111**, 117002 (2013). URL https://link.aps.org/doi/10.1103/PhysRevLett.111.117002.

[12] Fermin, R., de Wit, B. & Aarts, J. Beyond the effective length: How to analyze magnetic interference patterns of thin-film planar josephson junctions with finite lateral dimensions. Phys. Rev. B **107**, 064502 (2023). URL https://link.aps.org/doi/10.1103/PhysRevB.107.064502.

[13] Keizer, R. S. et al. A spin triplet supercurrent through the half-metallic ferromagnet CrO_2. Nature **439**, 825–827 (2006). URL https://doi.org/10.1038/nature04499.

[14] Anwar, M. S., Czeschka, F., Hesselberth, M., Porcu, M. & Aarts, J. Long-range supercurrents through half-metallic ferromagnetic CrO_2. Phys. Rev. B **82**, 100501 (2010). URL https://link.aps.org/doi/10.1103/PhysRevB.82.100501.

[15] Anwar, M. S., Veldhorst, M., Brinkman, A. & Aarts, J. Long range supercurrents in ferromagnetic CrO_2 using a multilayer contact structure. Applied Physics Letters **100**, 052602 (2012). URL https://doi.org/10.1063/1.3681138.

[16] Singh, A., Jansen, C., Lahabi, K. & Aarts, J. High-Quality CrO_2 Nanowires for Dissipation-less Spintronics. Physical Review X **6**, 041012 (2016).

[17] Koyama, T. et al. Observation of the intrinsic pinning of a magnetic domain wall in a ferromagnetic nanowire. Nature materials **10**, 194–197 (2011).

[18] Weiss, P. & Foex, G. Le Magnétism. Paris: Armand Colln (1926).

[19] Barkhausen, H. Zwei mit Hilfe der neuen Verstärker entdeckte Erscheinungen. Physische Zeitschrift **20**, 401–403 (1919).

[20] Sixtus, K. J. & Tonks, L. Propagation of Large Barkhausen Discontinuities. Phys. Rev. **37**, 930–958 (1931). URL https://link.aps.org/doi/10.1103/PhysRev.37.930.

[21] Bitter, F. Experiments on the Nature of Ferromagnetism. Phys. Rev. **41**, 507–515 (1932). URL https://link.aps.org/doi/10.1103/PhysRev.41.507.

[22] Landau, L. & Lifschitz, E. On the Theory of the Dispersion of Magnetic Permeability in Ferromagnetic Bodies. Physische Zeitschrift der Sowjetunion **8**, 153–169 (1935).

[23] Bloch, F. Zur Theorie des Austauschproblems und der Remanenzerscheinung der Ferromagnetika. Zeitschrift für Physik **74**, 295–335 (1932). URL https://doi.org/10.1007/BF01337791.

[24] Heisenberg, W. Zur Theorie der Magnetostriktion und der Magnetisierungskurve. Zeitschrift für Physik **69**, 287–297 (1931). URL https://doi.org/10.1007/BF01391350.

[25] Kittel, C. Physical Theory of Ferromagnetic Domains. Rev. Mod. Phys. **21**, 541–583 (1949). URL https://link.aps.org/doi/10.1103/RevModPhys.21.541.

[26] Hubert, A. & Schäfer, R. Magnetic Domains - The Analysis of Magnetic Microstructures (Springer Berlin, Heidelberg, 1998).

[27] O'Handley, R. C. Modern Magnetic Materials - Principles and Applications (John Wiley & Sons, Inc., 1999).

[28] Marrows, C. H. Spin-polarised currents and magnetic domain walls. Advances in Physics **54**, 585–713 (2005). URL https://doi.org/10.1080/00018730500442209.

[29] Zou, X. Magnetic Domain Configurations and Huge Wall Resistivity in Half-metallic Chromium Dioxide (CrO_2) Nanostructures. Ph.D. thesis, Brown University, Providence, Rhode Island, 5 (2010).

[30] Bertotti, G. Hysteresis in Magnetism (First Edition. Academic Press, San Diego, CA, USA, 1998).

[31] University of Birmingham, Magnetic Materials Group (2009). URL https://www.birmingham.ac.uk/research/activity/metallurgy-materials/magnets/Magnetic-Materials-Background-Information.aspx.

[32] Néel, L. Quelques propriétés des parois des domaines élémentaires ferromagnétiques. Cahiers de Physique **25**, 1–20 (1944).

[33] Slonczewski, J. Current-driven excitation of magnetic multilayers. Journal of Magnetism and Magnetic Materials **159**, L1–L7 (1996). URL https://www.sciencedirect.com/science/article/pii/0304885396000625.

[34] Coey, J. M. D. Magnetism and Magnetic Materials (Cambridge University Press, New York, 2010). URL http://www.cambridge.org/9780521816144.

[35] Estévez, V. & Laurson, L. Head-to-head domain wall structures in wide permalloy strips. Phys. Rev. B **91**, 054407 (2015). URL https://link.aps.org/doi/10.1103/PhysRevB.91.054407.

[36] Gilbert, T. A phenomenological theory of damping in ferromagnetic materials. IEEE Transactions on Magnetics **40**, 3443–3449 (2004).

[37] Berger, L. Low-field magnetoresistance and domain drag in ferromagnets. Journal of Applied Physics **49**, 2156–2161 (1978). URL https://doi.org/10.1063/1.324716. https://doi.org/10.1063/1.324716.

[38] Zhang, S. & Li, Z. Roles of Nonequilibrium Conduction Electrons on the Magnetization Dynamics of Ferromagnets. Phys. Rev. Lett. **93**, 127204 (2004). URL https://link.aps.org/doi/10.1103/PhysRevLett.93.127204.

[39] Simon, B. G. Domain wall motion in Permalloy nanowires. Master's thesis, Leiden University, Netherlands (2018).

[40] Li, Z. & Zhang, S. Domain-Wall Dynamics and Spin-Wave Excitations with Spin-Transfer Torques. Phys. Rev. Lett. **92**, 207203 (2004). URL https://link.aps.org/doi/10.1103/PhysRevLett.92.207203.

[41] Thiaville, A., Nakatani, Y., Miltat, J. & Vernier, N. Domain wall motion by spin-polarized current: a micromagnetic study. Journal of Applied Physics **95**, 7049–7051 (2004). URL https://doi.org/10.1063/1.1667804. https://doi.org/10.1063/1.1667804.

[42] Kläui, M. et al. Domain wall motion induced by spin polarized currents in ferromagnetic ring structures. Applied Physics Letters **83**, 105–107 (2003). URL https://doi.org/10.1063/1.1588736. https://doi.org/10.1063/1.1588736.

[43] Thiaville, A., Nakatani, Y., Miltat, J. & Suzuki, Y. Micromagnetic understanding of current-driven domain wall motion in patterned nanowires. Europhysics Letters **69**, 990 (2005). URL https://dx.doi.org/10.1209/epl/i2004-10452-6.

[44] Parkin, S. S. P., Hayashi, M. & Thomas, L. Magnetic Domain-Wall Racetrack Memory. Science **320**, 190–194 (2008). URL https://www.science.org/doi/abs/10.1126/science.1145799.

[45] Yamaguchi, A. et al. Real-space observation of current-driven domain wall motion in submicron magnetic wires. Phys. Rev. Lett. **92**, 077205 (2004). URL https://link.aps.org/doi/10.1103/PhysRevLett.92.077205.

[46] Kläui, M. et al. Controlled and reproducible domain wall displacement by current pulses injected into ferromagnetic ring structures. Phys. Rev. Lett. **94**, 106601 (2005). URL https://link.aps.org/doi/10.1103/PhysRevLett.94.106601.

[47] Hayashi, M. et al. Dependence of Current and Field Driven Depinning of Domain Walls on their Structure and Chirality in Permalloy Nanowires.

Phys. Rev. Lett. **97**, 207205 (2006). URL https://link.aps.org/doi/10.1103/PhysRevLett.97.207205.

[48] Meier, G. et al. Direct imaging of stochastic domain-wall motion driven by nanosecond current pulses. Phys. Rev. Lett. **98**, 187202 (2007). URL https://link.aps.org/doi/10.1103/PhysRevLett.98.187202.

[49] Tatara, G. & Kohno, H. Theory of Current-Driven Domain Wall Motion: Spin Transfer versus Momentum Transfer. Phys. Rev. Lett. **92**, 086601 (2004). URL https://link.aps.org/doi/10.1103/PhysRevLett.92.086601.

[50] Koch, R. H., Katine, J. A. & Sun, J. Z. Time-resolved reversal of spin-transfer switching in a nanomagnet. Phys. Rev. Lett. **92**, 088302 (2004). URL https://link.aps.org/doi/10.1103/PhysRevLett.92.088302.

[51] Sun, J. Z. Spin-current interaction with a monodomain magnetic body: A model study. Phys. Rev. B **62**, 570–578 (2000). URL https://link.aps.org/doi/10.1103/PhysRevB.62.570.

[52] Hayashi, M. et al. Current Driven Domain Wall Velocities exceeding the Spin Angular Momentum Transfer Rate in Permalloy Nanowires. Phys. Rev. Lett. **98**, 037204 (2007). URL https://link.aps.org/doi/10.1103/PhysRevLett.98.037204.